Microscopic Eilenberger theory of Fulde-Ferrell-Larkin-Ovchinnikov states in the presence of vortices

Kenta M. Suzuki
Department of Physics, Okayama University, Okayama 700-8530, Japan

Kazushige Machida
Department of Physics, Ritsumeikan University, Kusatsu 525-8577, Japan

Yasumasa Tsutsumi*
RIKEN Center for Emergent Matter Science, Wako, Saitama 351-0198, Japan

Masanori Ichioka
Department of Physics, Okayama University, Okayama 700-8530, Japan
and Research Institute for Interdisciplinary Science, Okayama University, Okayama 700-8530, Japan

(Received 1 March 2020; revised manuscript received 27 May 2020; accepted 28 May 2020; published 12 June 2020)

We theoretically investigate the Fulde-Ferrell-Larkin-Ovchinnikov state by using the microscopic quasiclassical Eilenberger equation. The Pauli paramagnetic effects and the orbital depairing effects due to vortices are treated on an equal footing for three-dimensional spherical Fermi surface model and *s*-wave pairing. The field evolution of the Larkin-Ovchinnikov (LO) state is studied in detail, such as the H-T phase diagram, spatial structures of the order parameter, the paramagnetic moment, and the internal field. Field dependences of various thermodynamic quantities—the paramagnetic moment, entropy, and the zero-energy density of states—are calculated. Those quantities are shown to start quickly growing upon entering the LO state. We also evaluate the wavelength of the LO modulation, the flux line lattice form factors for small-angle neutron scattering, and the NMR spectra to facilitate the identification of the LO state. Two cases of strong and intermediate Pauli paramagnetic effect are studied comparatively. The possibility of the LO phase in Sr_2RuO_4, $CeCoIn_5$, $CeCu_2Si_2$, and the organic superconductors is critically examined and crucial experiments to identify it are proposed.

DOI: 10.1103/PhysRevB.101.214516

I. INTRODUCTION

In 1964, Fulde and Ferrell (FF) [1] and Larkin and Ovchinnikov (LO) [2] proposed a theoretical possibility of a spatially modulated superconducting state [3] under the Zeeman effect. Since then, there have been many works focusing on the realization of the Fulde-Ferrell-Larkin-Ovchinnikov (FFLO) state both theoretically and experimentally. Yet there is no well-accepted material where the FFLO state is realized.

In the FFLO state, the superconducting order parameter in the singlet pairing, such as *s*-wave or *d*-wave pairing, exhibits a spatial modulation [3]. Under the population imbalance of up- and down-spin species of Cooper pairs, it is expected that the FFLO state is the most possible state to emerge [4,5]. The population imbalance is brought about either by its preparation in cold neutral atom gases [6–8] or by application of an external field in the charged particle case through the Pauli paramagnetic effect.

One of the reasons for the difficulties in realizing the FFLO state in a superconductor may come from the lack of theoretical investigations which fully take into account both the Pauli paramagnetic effect and the flux line effect on an equal footing. The simultaneous consideration of the two depairing effects, paramagnetic depairing in the former and orbital depairing in the latter, is a difficult task because the two kinds of spatial modulations—one due to the FFLO state and the other to flux line lattice—must be handled simultaneously. It is often the case [9–13] only to consider the Pauli paramagnetic effect by neglecting the latter effect, including the original works by Fulde and Ferrell [1] and Larkin and Ovchinnikov [2]. In those studies the *s*-wave [9,10] and *d*-wave [11–13] pairing cases are treated. The attempts to simultaneously consider the two effects are limited to the so-called Ginzburg-Landau (GL) region near H_{c2} [14–16]. Thus we need more extensive studies which cover the whole region of T and H. This is one of the main purposes of our present paper.

The LO state with periodically modulated amplitude of the order parameter is far more difficult to describe due to the so-called solitonic spatial variation with infinitely many higher harmonics of the Fourier component of the order parameter

*Present address: Department of Physics, Kwansei Gakuin University, Sanda, Hyogo 669-1337, Japan.

in general. This is handled exactly and analytically [10] only in the absence of the orbital depairing. The LO state is so computationally demanding, but it is stabler than the FF state where only the phase is modulated in the order parameter [10]. Thus we consider the LO state in this paper. There are two possible modulation directions with respect to the applied magnetic field: the modulation is along the field direction, or perpendicular to it. In this paper, we consider the former LO state which is expected to be stabler than the latter LO state physically.

Thus the main purpose of this paper is to provide fundamental theoretical information on the physical properties of the LO states. In particular, we study how the field evolutions of various observables are, including thermodynamic quantities, such as the entropy, the zero-energy density of states (DOS) measured by low-temperature specific heat experiment, and magnetization changes. We also calculate the flux line lattice (FLL) form factors measured by small-angle neutron scattering (SANS), and the nuclear magnetic resonance (NMR) spectrum in the LO state.

For that purpose, to obtain the magnetic field H dependence of the LO states by advancing our previous study [17], we solve the microscopic Eilenberger equation fully self-consistently in three-dimensional (3D) space of vortex and LO modulation [17], and find the free energy minimum with respect to the LO period L. The orbital depairing and Pauli paramagnetic depairing are treated on an equal footing here. The phase diagram in the H-T plane is constructed where the Abrikosov phase and the LO phase are competing, and we examine the behaviors of the various observables mentioned above. In this paper, we compare two cases of strong and intermediate Pauli paramagnetic effect.

Our basic strategy is to study the canonical field-dependent properties of the LO states for a spherical Fermi surface model and s-wave pairing. The corresponding 3D calculation for the FF state [9] and full self-consistent analytic theory for a quasi-one-dimensional (quasi-1D) case [10] have been performed before without vortices. Here we extend their calculations to take into account the vortex effects. The effects of the d-wave pairing on the LO state within the same Eilenberger framework were reported [17].

There are several important and outstanding experimental results to suggest that the LO state remains unexplored in detail because of the lack of appropriate theoretical methods to describe further detailed behaviors of the LO state. For example:

(1) NMR experiments on $CeCoIn_5$ where the resonance spectra exhibit a characteristic signature and change when entering the high field LO state [18–20]. And specific heat studies on $CeCoIn_5$ for $H \parallel ab$ exhibit a characteristic first-order transition [21]. Neutron experiments [22,23] detect anomalous magnetism, the so-called Q phase in the high field region for $H \parallel ab$.

(2) Small-angle neutron-scattering experiments have been done for $CeCoIn_5$ of $H \parallel c$ [24,25] where the FLL form factor $|F_{100}(H)|$ increases toward H_{c2} contrary to the ordinary type II superconductors which exhibit a rapid decrease as H increases. Just before H_{c2}, $|F_{100}(H)|$ sharply drops to zero.

(3) In κ-$(BEDT\text{-}TTF)_2Cu(NCS)_2$, Mayaffre *et al.* [26] find a sharp increase of T_1^{-1} as a function of H and T near and just below H_{c2} when entering the high field phase, suggesting the LO state in this quasi-2D superconductor.

(4) However, in $CeCu_2Si_2$ [27] a similar T_1^{-1} enhancement phenomenon is reported. In our opinion it is unrelated to the LO, although the authors claim it is because of the reasons given in Ref. [28]. Thus it is obvious that we definitely need a careful theoretical study to firmly identify the LO state, which is able to check various aspects of the LO signatures, not only a single phenomenon such as the T_1^{-1} enhancement, but also the consistency with other phenomena associated with the LO state to avoid further confusion.

(5) Sr_2RuO_4 was a prime candidate for a chiral p-wave superconductor [29,30], but recent various theoretical and experimental studies [31–33] indicate now that it is most likely to be a spin-singlet superconductor. The system well satisfies the necessary conditions for the LO state to appear. Namely, it is superclean in that (a) the mean free path l must be longer than the periodicity L of the LO state, which is typically an order of 100ξ with ξ coherence length (see later for details), that is, $l \gg L$. (b) Favorably, it is low dimensional, and (c) has a strong Pauli paramagnetic effect to avoid the orbital depairing. Thus this is enough reason to investigate the LO state in this material, which is true for other materials, $CeCoIn_5$ and κ-$(BEDT\text{-}TTF)_2Cu(NCS)_2$, but not for $CeCu_2Si_2$ which is known to be a barely clean system, namely, $l \sim \xi$ and three-dimensional electronic structure, although the Pauli paramagnetic effect is sufficiently strong [28].

The plan of this paper is as follows. We first introduce our formulation based on the microscopic quasiclassical Eilenberger framework [34] in Sec. II. This formulation is valid for $\xi k_F \gg 1$ with k_F the Fermi wave number, which is well satisfied for the materials of interest. The LO phase diagram in the H vs T plane is determined in Sec. III. The spatial structure of the LO state is examined in Sec. IV. The field evolutions of thermodynamic quantities mentioned above are presented in Sec. V. Those are accessible by a variety of experimental methods. The FLL form factors with various indices and NMR spectra are calculated in Sects. VI and VII, respectively. Throughout this paper, we treat the two cases $\mu = 5$ and $\mu = 2$ comparatively, corresponding to the strong and intermediate Pauli paramagnetic effect cases where μ is a measure of the strength of the Zeeman effect, related to the so-called Maki parameter $\alpha_{\rm Maki}$ through $\mu = 2\alpha_{\rm Maki}$, which is defined by $\alpha_{\rm Maki} = \sqrt{2}H_{c2}^{\rm orb}/H_p$ with $H_{c2}^{\rm orb}$ being the orbital limiting upper critical field and H_p the Pauli limiting critical field [3]. In Sect. VIII, we critically examine each candidate material for the possible realization of the LO state in light of the present calculation and propose further experiments to firmly establish and identify the LO state. We devote the last section to our conclusions. A part of the present results is reported in Ref. [35].

II. FORMULATION FOR EILENBERGER THEORY

We calculate the 3D spatial structure of the vortex lattice state by using the quasiclassical Eilenberger theory in the clean limit [36–39], assuming that the order parameter modulates along the magnetic field direction in the LO state. The Pauli paramagnetic effects are included through the Zeeman term $\mu_B B(\mathbf{r})$, where $B(\mathbf{r})$ is the flux density of the internal

field and μ_B is a renormalized Bohr magneton. The quasiclassical Green's functions $g(\omega_n + i\mu B, \mathbf{k}, \mathbf{r})$, $f(\omega_n + i\mu B, \mathbf{k}, \mathbf{r})$, and $f^\dagger(\omega_n + i\mu B, \mathbf{k}, \mathbf{r})$ are calculated in the vortex lattice state by the Eilenberger equations [17,36–40]

$$\begin{aligned}\{\omega_n + i\mu B + \tilde{\mathbf{v}} \cdot (\boldsymbol{\nabla} + i\mathbf{A})\} f &= \Delta g,\\ \{\omega_n + i\mu B - \tilde{\mathbf{v}} \cdot (\boldsymbol{\nabla} - i\mathbf{A})\} f^\dagger &= \Delta^* g,\end{aligned} \tag{1}$$

where $g = (1 - ff^\dagger)^{1/2}$, $\mathrm{Re} g > 0$, $\tilde{\mathbf{v}} = \mathbf{v}/v_{\mathrm{F0}}$, and the Pauli parameter $\mu = \mu_B B_0/\pi k_B T_c$. $\mathbf{k}$ is the relative momentum of the Cooper pair, and $\mathbf{r}$ is the center-of-mass coordinate of the pair. $\mathbf{v}$ is the Fermi velocity and $v_{\mathrm{F0}} = \langle v^2 \rangle_{\mathbf{k}}^{1/2}$ where $\langle \cdots \rangle_{\mathbf{k}}$ indicates the Fermi surface average. An isotropic spherical Fermi surface is considered in this study. We assume that a magnetic field is applied to the z axis. The Eilenberger units $R_0 = \hbar v_{\mathrm{F0}}/2\pi k_B T_c$ for lengths and $B_0 = \hbar c/2|e|R_0^2$ for magnetic fields are used [17,40]. The order parameter Δ and the Matsubara frequency ω_n are normalized in units of $\pi k_B T_c$.

As for self-consistent conditions, the order parameter is calculated by

$$\Delta(\mathbf{r}) = g_0 N_0 T \sum_{0<\omega_n \leqslant \omega_{\mathrm{cut}}} \langle f + f^{\dagger *} \rangle_{\mathbf{k}} \tag{2}$$

with $(g_0 N_0)^{-1} = \ln T + 2T \sum_{0<\omega_n \leqslant \omega_{\mathrm{cut}}} \omega_n^{-1}$. We use $\omega_{\mathrm{cut}} = 20 k_B T_c$. $\mathbf{B} = \boldsymbol{\nabla} \times \mathbf{A}$ with the vector potential $\mathbf{A} = \frac{1}{2}\bar{\mathbf{B}} \times \mathbf{r} + \mathbf{a}$ and $\bar{\mathbf{B}} = (0, 0, \bar{B})$. $\bar{B}$ is the averaged flux density of the internal field, and $\langle \boldsymbol{\nabla} \times \mathbf{a} \rangle_{\mathbf{r}} = 0$. The spatial variation of the internal field $\boldsymbol{\nabla} \times \mathbf{a}$ is self-consistently determined by

$$\boldsymbol{\nabla} \times (\boldsymbol{\nabla} \times \mathbf{a}) = \boldsymbol{\nabla} \times \mathbf{M}_{\mathrm{para}}(\mathbf{r}) - \frac{2T}{\kappa^2} \sum_{0<\omega_n} \langle \tilde{\mathbf{v}}\, \mathrm{Im}\, g \rangle_{\mathbf{k}}, \tag{3}$$

where we consider both the contribution of the paramagnetic moment and the diamagnetic contribution of supercurrent in the second term. Thus from Eq. (3) the paramagnetic moment with $\mathbf{M}_{\mathrm{para}}(\mathbf{r}) = [0, 0, M_{\mathrm{para}}(\mathbf{r})]$ is given by [17,41]

$$M_{\mathrm{para}}(\mathbf{r}) = M_0 \left(\frac{B(\mathbf{r})}{\bar{B}} - \frac{2T}{\mu \bar{B}} \sum_{0<\omega_n} \langle \mathrm{Im}\, g \rangle_{\mathbf{k}} \right). \tag{4}$$

Namely, the paramagnetic moment consists of the normal-state part in the first term and the compensation part by the superconducting state in the second term. The normal-state paramagnetic moment $M_0 = (\mu/\kappa)^2 \bar{B}$, $\kappa = B_0/\pi k_B T_c \sqrt{8\pi N_0}$, and N_0 is the DOS at the Fermi energy in the normal state. We set the GL parameter $\kappa = 102$. Using the spatial averaged value $M_{\mathrm{para}} = \langle M_{\mathrm{para}}(\mathbf{r}) \rangle_{\mathbf{r}}$, the normalized paramagnetic susceptibility is given by $\chi_{\mathrm{spin}} = M_{\mathrm{para}}/M_0$.

In the Eilenberger theory, the Gibbs free energy is given by [42]

$$\begin{aligned}F = &\left\langle \kappa^2 |\mathbf{B}(\mathbf{r}) - \mathbf{H}|^2 - \mu^2 |B(\mathbf{r})|^2 \right\rangle_{\mathbf{r}}\\ &+ T \sum_{|\omega_n| < \omega_{\mathrm{cut}}} \left\langle \mathrm{Re} \left\langle \frac{g-1}{g+1} (\Delta f^\dagger + \Delta^* f) \right\rangle_{\mathbf{k}} \right\rangle_{\mathbf{r}}.\end{aligned} \tag{5}$$

$\langle \cdots \rangle_{\mathbf{r}}$ indicates the spatial average within a unit cell of the vortex lattice. The entropy in the superconducting state, given by $S_s(T) = S_n(T) - \partial F/\partial T$, is obtained as [42]

$$\begin{aligned}\frac{S_s(T)}{S_n(T_c)} = T - \frac{3}{2} \sum_{0<\omega_n<\omega_{\mathrm{cut}}} \mathrm{Re} \Bigg\langle \Bigg\langle & g_0 N_0 (\Delta f^\dagger + \Delta^* f)\\ & - 2\frac{\Delta f^\dagger + \Delta^* f}{g+1} - 4\omega_n (g-1) \Bigg\rangle_{\mathbf{k}} \Bigg\rangle_{\mathbf{r}},\end{aligned} \tag{6}$$

where S_n is the entropy in the normal state.

We obtain the relation of $\bar{B}$ and the external field H as

$$\begin{aligned}H = &\left(1 - \frac{\mu^2}{\kappa^2}\right) \left(\bar{B} + \frac{1}{\bar{B}} \langle (B(\mathbf{r}) - \bar{B})^2 \rangle_{\mathbf{r}} \right)\\ &+ \frac{T}{\kappa^2 \bar{B}} \sum_{0<\omega_n} \Bigg\langle \Bigg\langle \mu B(\mathbf{r}) \mathrm{Im}\{g\} + \frac{1}{2} \mathrm{Re} \left\{ \frac{(f^\dagger \Delta + f \Delta^*) g}{g+1} \right\}\\ &+ \omega_n \mathrm{Re}\{g - 1\} \Bigg\rangle_{\mathbf{k}} \Bigg\rangle_{\mathbf{r}}\end{aligned} \tag{7}$$

from Doria-Gubernatis-Rainer scaling [41,43]. In the parameters used in our calculation, $|\bar{B} - H| < 10^{-4} B_0$. The magnetization is calculated as $M = \bar{B} - H$, which includes the paramagnetic component M_{para} in addition to the diamagnetic contributions.

In the self-consistent Eilenberger theory, we solve Eq. (1) and Eqs. (2)–(4) alternately, and obtain self-consistent solutions of $\Delta(\mathbf{r})$, $\mathbf{A}(\mathbf{r})$, and quasiclassical Green's functions with ω_n, as in previous works [17,40] under a given unit cell of the triangular vortex lattice. Using the self-consistent solutions, we evaluate the free energy in Eq. (5), the entropy in Eq. (6), and the external field in Eq. (7).

For the LO state, $\Delta(\mathbf{r})$ has periodic oscillation of the period L along the z axis of the vortex line, in addition to the vortex lattice structure in the xy plane. The unit cell of the vortex lattice is given by $(x, y) = u_1(\mathbf{r}_1 - \mathbf{r}_2) + u_2 \mathbf{r}_2$ with $-0.5 \leqslant u_i \leqslant 0.5$ $(i = 1, 2)$. $\mathbf{r}_1 = (c_x, 0, 0)$ and $\mathbf{r}_2 = (c_x/2, c_y, 0)$ with $c_x c_y \bar{B} = \phi_0$ and the flux quantum ϕ_0. As the unit cell size of the vortex lattice is determined by $\bar{B} \sim H$, we can estimate the H dependence of the LO states in our calculation of the vortex lattice. We use $\mu = 5$ and $\mu = 2$ as representative cases of strong and intermediate Pauli paramagnetic effect, respectively.

When we calculate the electronic state, we solve Eq. (1) with $i\omega_n \to E + i\eta$. In the calculation we use $\Delta(\mathbf{r})$, $\mathbf{A}(\mathbf{r})$, and $B(\mathbf{r})$ which are obtained from the above self-consistent calculation. η is an infinitesimal constant. From the quasiclassical Green's function of real energy E, the DOS is given by $N(E) = [N_{+1}(E) + N_{-1}(E)]/2$ with

$$N_\sigma(E) = N_0 \mathrm{Re} \langle \langle g(\omega_n + i\sigma\mu B, \mathbf{k}, \mathbf{r})|_{i\omega_n \to E + i\eta} \rangle_{\mathbf{k}} \rangle_{\mathbf{r}} \tag{8}$$

with $\sigma = +1$ (-1) for the up- (down-) spin component. We study the H dependence of the Sommerfeld coefficient $\gamma(H)$ of the low-temperature specific heat. This is given by the normalized zero-energy DOS as $\gamma(H) = N(E = 0)/N_0$.

III. PHASE DIAGRAM

Before studying the thermodynamic quantities in the LO state mentioned above, we evaluate the phase diagram of the LO state, and the stable LO period L as a function of H.

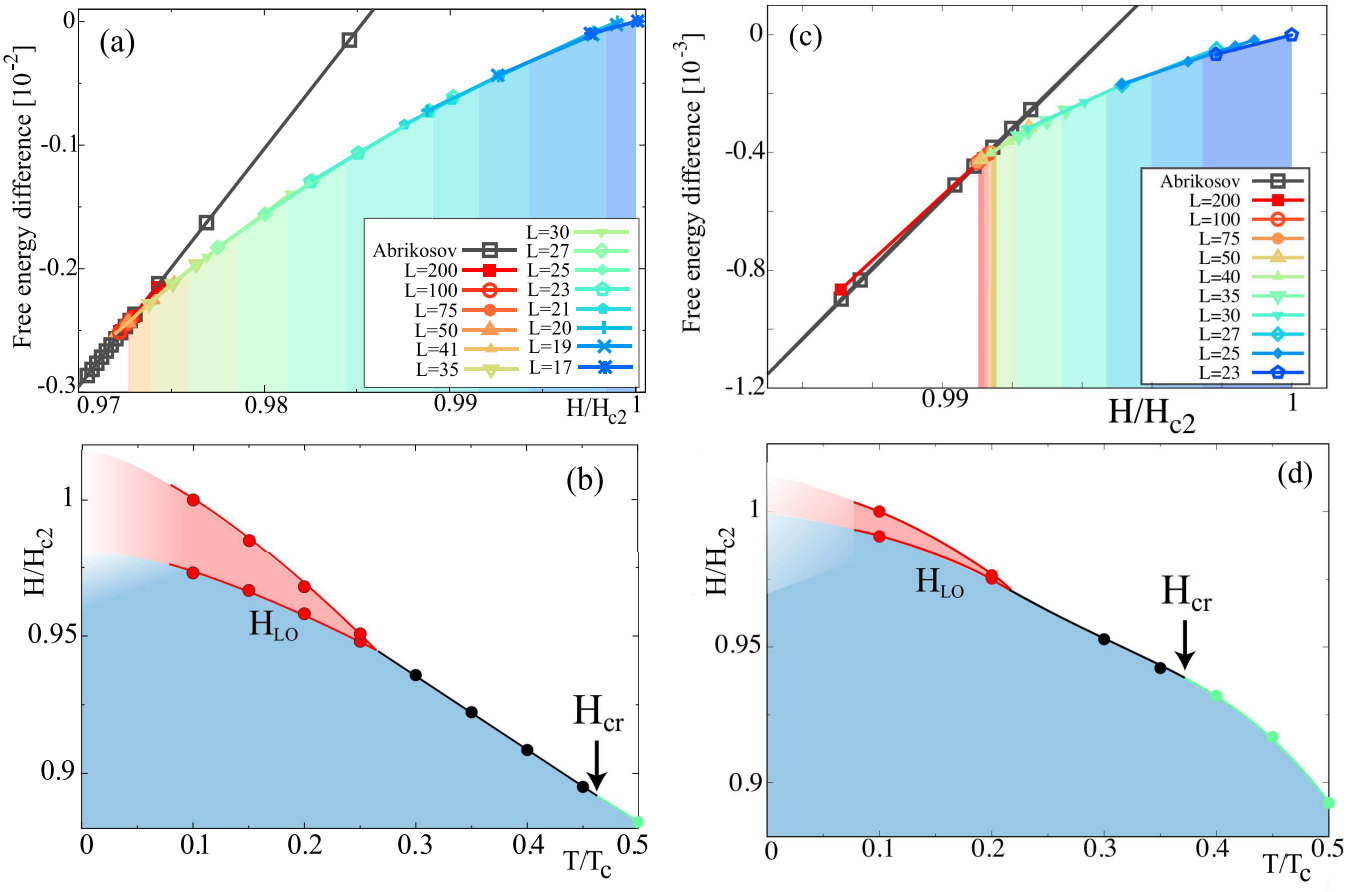

FIG. 1. (a) and (c) Free energies F of the LO states with different wave numbers L and Abrikosov state relative to the normal state as a function of H for $\mu = 5$ and $\mu = 2$, respectively, at $T = 0.1T_c$. With increasing H toward H_{c2}, the LO states with shorter spatial periodicity L indicated by different color bars are stabilized successively. (b) and (d) Phase diagrams for LO in the H-T plane for $\mu = 5$ and $\mu = 2$, respectively. H is normalized by H_{c2} at $T = 0.1T_c$. The upper red region is the LO phase where the vortex lattice state with the LO modulation along the field direction is stabilized. The blue regions in the lower fields correspond to the Abrikosov vortex lattice state without the LO modulation. The boundary H_{LO} is second-order transition. H_{c2} is first-order transition for $H > H_{cr}$, while it is second-order transition for $H < H_{cr}$. Lines are guides for the eyes.

The Gibbs free energy in Eq. (5) is calculated from self-consistent solutions of Eq. (2) for the LO states with various LO wavelength L normalized by R_0. We compare them to find the most stable state under a given H and T.

Figures 1(a) for $\mu = 5$ and 1(c) for $\mu = 2$ exhibit the resulting successive changes of F and L at $T/T_c = 0.1$. At around $H = H_{c2}$ the LO state with the shortest wavelength is stabilized, which is $L \sim 17$ for $\mu = 5$ and $L \sim 23$ for $\mu = 2$. Note that the length unit R_0 is roughly equal to the coherence length ξ_0. As H decreases, L becomes longer and longer. Eventually the free energy of the LO state becomes comparable with that of the Abrikosov state where the LO modulation along the field direction is absent. The envelope of the free energies of the LO state approaches that of the Abrikosov state, such that the two curves seem to merge tangentially, namely, at the meeting point the tangents of the two curves coincide with each other. As seen later, the thermodynamic quantities exhibit sharp kink behaviors at H_{LO} reminiscent of first-order transition, but we think it second order because of those free energy behaviors. While our calculations are done for discretized L, these results suggest second-order-like transition at H_{LO} [16] and the continuous L change as a function of H in the LO state $H_{LO} < H < H_{c2}$, similar to the results of a previous analytic LO theory [10]. H_{LO} is the transition field from the Abrikosov vortex state to the LO state.

We also notice here that as seen from Figs. 1(a) and 1(c) the Abrikosov state shows the first-order transition if the LO state is absent. Then the LO states enhance the upper critical field H_{c2} substantially. The superconducting state survives to higher fields by creating the LO states. The enhancement is larger for $\mu = 5$ than for $\mu = 2$.

In Figs. 1(b) for $\mu = 5$, and 1(d) for $\mu = 2$, we show the resulting phase diagrams in the H-T plane. Those are obtained by repeating the LO calculations as a function of H at different temperatures $T/T_c = 0.1$, 0.15, 0.2, and 0.25 for $\mu = 5$, and $T/T_c = 0.1$ and 0.2 for $\mu = 2$. We show the critical point (T_{cr}, H_{cr}) in Figs. 1(b) and 1(d) where H_{cr} is determined by solving the equation for H_{c2}. The transition at H_{c2} to the normal state is first order at $H > H_{cr}$.

It is seen that in the strong paramagnetic case $\mu = 5$ in Fig. 1(b), the LO phase appears only near H_{c2}, and H_{LO} increases on lowering T in this typical example of an isotropic Fermi sphere. As for the $\mu = 2$ case in Fig. 1(d), the basic

features of the phase diagram are essentially the same as $\mu = 5$ except that the LO phase shrinks and becomes narrower. The LO region in the H-T plane is given by $H_{\rm LO}/H_{c2} = 0.973$ for $\mu = 5$ at $T/T_c = 0.1$, which depends on the μ value, namely, $H_{\rm LO}/H_{c2} = 0.991$ for $\mu = 2$ at $T/T_c = 0.1$. To obtain a wider LO region, we have to consider the contribution of a realistic Fermi surface shape such as a quasi-2D shape [17] for better nesting condition, or multiband effect [44,45].

Those phase diagrams are different from those for the Zeeman depairing without the orbital depairing [10] and also for the neutral Fermi superfluids with spin imbalance [5]. In the former case H_{c2} of the LO phase shifts to much higher fields, while a much wider LO phase is obtained in the latter case.

We notice the canonical phase diagram [10], consisting of the second-order line at higher T, which bifurcates into two second-order lines at lower T in the theory without considering first-order transition. In the present calculation, we show how the phase diagram changes in the presence of first-order transition. The bifurcation point is known as the tricritical point, the so-called Lifshitz point $H_{\rm Lifshitz}$ [10,46]. According to the canonical phase diagram [10,46], it is expected that $H_{\rm cr}$ should coincide with the end point of the $H_{\rm LO}$ line, namely, the LO phase starts from $H_{\rm cr}$. However, we note that within our numerics, it is not determined whether or not the LO state extends to $H_{\rm cr}$. It is known that $T_{\rm LO}/T_{c2} = 0.56$ in the limit of $\mu \to \infty$. Thus we understand that the $\mu = 5$ case almost approaches the strong Pauli paramagnetic effect limit because $T_{\rm cr} \sim 0.48T_{c2}$ and the $\mu = 2$ case is intermediate because $T_{\rm cr} \sim 0.38T_{c2}$.

Here we mention a related theory [47] on the phase diagram of the FF state with a different approximation for the same 3D Fermi surface model. Similar to our approach, Ref. [47] has exploited the Gorkov Green's function theory in the quasiclassical approximation. Both theories have used nonperturbative methods of solution, with Ref. [47] presenting a direct analytical solution of Gorkov's equations, whereas here a numerical solution of the corresponding Eilenberger equation is performed. Reference [47] finds a second-order phase transition from the FF state to the normal state, and a first-order transition from the FF state to the Abrikosov state. The conclusion differs from ours for reasons unknown to us. We speculate that it might be due to the difference between FF and LO states, in addition to the difference of material parameters used in the calculations.

IV. SPATIAL STRUCTURE OF THE LO STATE

We investigate the three-dimensional spatial structures of various quantities in the LO states. Figure 2(a) displays the spatial profiles of the order parameter $\Delta(x, z)$ whose sign alternates along the z direction. At $z = 0$ the order parameter amplitude vanishes where the paramagnetic moment $M_{\rm para}(\mathbf{r})$ builds up in addition to the vortex core at $x = 0$ as shown in Fig. 2(b). The LO nodal kink forms a sheet of the paramagnetic moments perpendicular to the field. The magnetic induction field B_z is large along the vortex core at $x = 0$ and suppressed at the domain wall of the LO at $z = 0$. These B_z distributions indicate the confinement of B_z at the vortex core is weak at the LO nodal line.

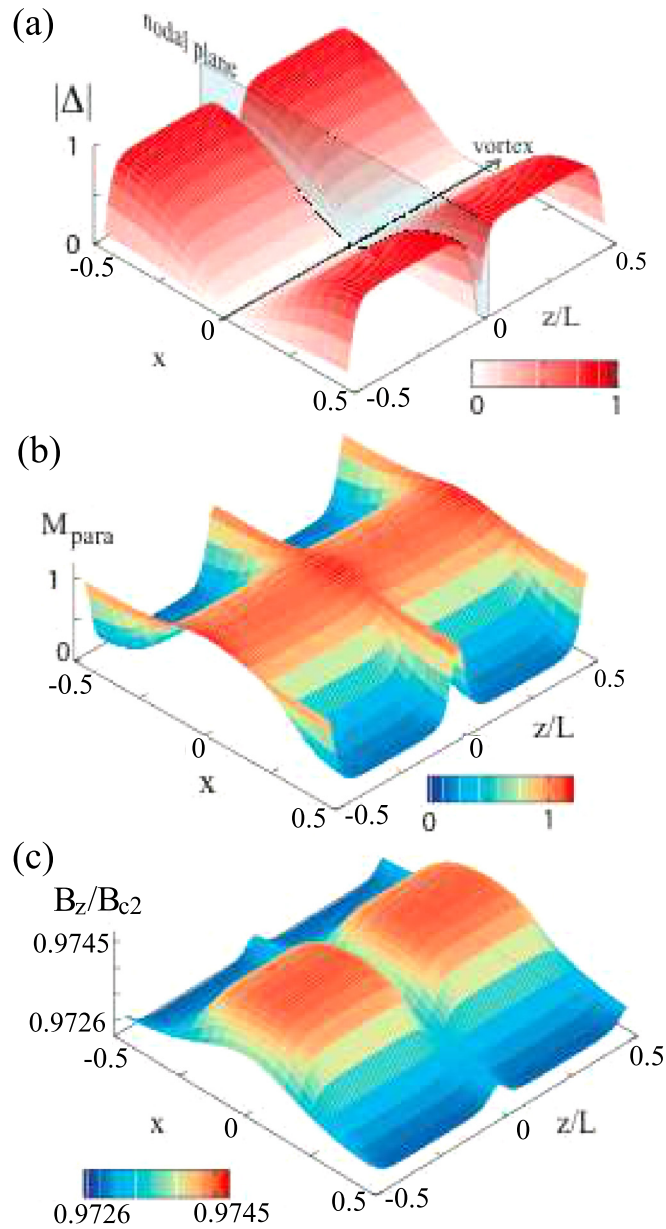

FIG. 2. Three-dimensional spatial profiles of (a) the order parameter $|\Delta(x, z)|$ normalized by the maximum value $|\Delta(x = 0.5c_x, z = 0.25L)|$, (b) paramagnetic moment $M_{\rm para}(x, z)/M_0$, and (c) induction field $B_z(x, z)$ normalized by $B_{c2}(T/T_c = 0.1)$. $T/T_c = 0.1$, $L = 75$, $H = 0.973H_{c2}$, and $\mu = 5$. The nodal planes are situated at $z/L = -0.5, 0, +0.5$ and the vortex center at $x = 0$. The profiles are displayed in one unit cell, $-0.5 \leqslant x/c_x \leqslant 0.5$ and $-0.5 \leqslant z/L \leqslant 0.5$.

The paramagnetic moment becomes strongly confined to the kink position as H approaches $H_{\rm LO}$ from the above. This is seen also from Fig. 3 more clearly. These features of the three-dimensional LO spatial structure can be probed by SANS experiment or NMR experiment.

Figure 3 shows the cross-sectional views of the normalized wave forms of the order parameter $\Delta(x = \pm 0.5c_x, z)$ (a) and paramagnetic moment $M_{\rm para}(x = \pm 0.5c_x, z)$ (b) in LO states along the field direction outside of the vortex core region where $x = \pm 0.5c_x$ are midpoints between nearest-neighbor vortices. It is seen that a simple sinusoidal modulation wave

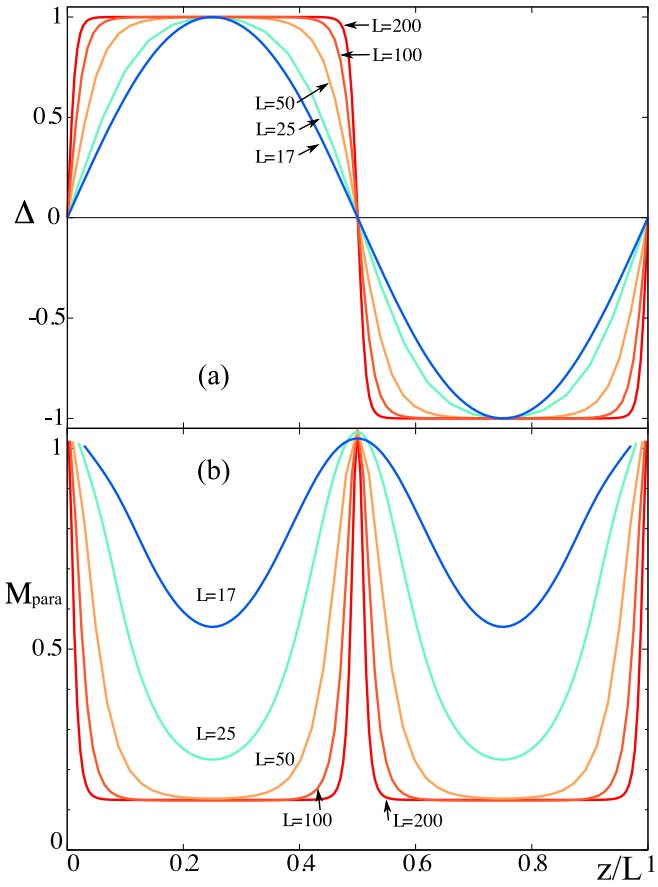

FIG. 3. Cross-sectional views of (a) the order parameter $\Delta(x = \pm 0.5c_x, z)$ normalized by the maximum value $|\Delta(x = 0.5c_x, z = 0.25L)|$, and (b) paramagnetic moment $M_{\rm para}(x = \pm 0.5c_x, z)/M_0$ for various wave numbers L along field direction z outside of the vortex core region at $x = \pm 0.5c_x$ and $y = 0$. $T/T_{\rm c} = 0.1$ and $\mu = 5$.

form for $L = 17$ stabilized near $H_{\rm c2}$ continuously deforms into an antiphase kink form, or solitonic wave form as H approaches the $H_{\rm LO}$ line, at which L diverges [10,46]. In other words, near the $H_{\rm LO}$ boundary, the sign change or π phase shift of the order parameter occurs sharply. For the longer L near $H_{\rm LO}$ due to the excess normal electrons $M_{\rm para}(\mathbf{r})$ is confined in a narrow spatial region along the kink position as clearly seen from Fig. 3(b). For shorter L approaching H_{c2}, $M_{\rm para}(\mathbf{r})$ is changed to a sinusoidal wave form. These changes of the LO structure reflect the behaviors of FLL form factors and NMR spectra, as discussed later.

V. FIELD EVOLUTIONS OF THERMODYNAMIC QUANTITIES

Thermodynamic quantities, such as magnetization curve $M_{\rm para}(H)$ and the Sommerfeld coefficient $\gamma(H)$ under the Pauli paramagnetic effect in the Abrikosov state, are evaluated in previous studies [48–51]. Here we continue those into the LO state, which takes over the Abrikosov phase in higher fields.

A. Magnetization

Figures 4(a) and 4(e) show magnetization curve $M = \bar{B} - H$ at $T = 0.1T_{\rm c}$ for $\mu = 5$ and $\mu = 2$, respectively. The magnetization M includes paramagnetic and diamagnetic contributions. As seen in the insets, $M < 0$ at low H as the diamagnetic contribution is dominant. If the Pauli paramagnetic effect is absent, $M \to 0$ when $H \to H_{\rm c2}$. However, in the presence of the Pauli paramagnetic effect, M becomes positive at high fields since the paramagnetic component $M_{\rm para}$ becomes dominant. Due to the larger paramagnetic contribution, M is larger for $\mu = 5$, compared with that for $\mu = 2$. In the Abrikosov state below $H < H_{\rm LO}$, M monotonically increases with a slow slope. When the Abrikosov state is changed to the LO state at $H > H_{\rm LO}$, we see a rapid increase of M. In Fig. 4, we plot data points for some L near free energy minimum. The continuous curves are drawn as a guide for the eyes. On the curves, the diverging slope at $H_{\rm LO}$ is gradually changed to a slower slope both for $\mu = 5$ and $\mu = 2$. In the narrow field region $H_{\rm LO} < H < H_{\rm c2}$, M increases toward the normal state value M_0 at $H > H_{\rm c2}$. The increase is larger for larger μ. We see a small jump of M at $H_{\rm c2}$. Although we expect a large jump of M at $H_{\rm c2}$ in the Abrikosov state if the LO state is absent, the jump is smeared by the increase of M due to the presence of the LO state at $H_{\rm LO} < H < H_{\rm c2}$.

B. Paramagnetic susceptibility

The H dependence of the normalized paramagnetic susceptibility $\chi_{\rm spin} = M_{\rm para}/M_0$ is presented in Figs. 4(b) and 4(f) for $\mu = 5$ and $\mu = 2$, respectively. The extrapolation of lines for $\chi_{\rm spin}$ in the Abrikosov state toward higher H until $\chi_{\rm spin} = 1$ suggests the orbital limit of $H_{\rm c2}$. The higher $H_{\rm c2}$ of the orbital limit is suppressed by the Pauli paramagnetic effect, and $\chi_{\rm spin}$ shows jump at the first-order $H_{\rm c2}$ transition, as shown in Figs. 4(b) and 4(f). The jump is larger for larger μ. Since the dominant contribution of M comes from the paramagnetic part $M_{\rm para}$ at high fields, $M_{\rm para}$ in Figs. 4(b) and 4(f) shows similar behavior to M in Figs. 4(a) and 4(e) in the LO state. $\chi_{\rm spin}$ also shows a large increase in the LO state at $H_{\rm LO} < H < H_{\rm c2}$, and a small jump to $\chi_{\rm spin} = 1$ at $H_{\rm c2}$. In the LO state, $\chi_{\rm spin}$ changes from 0.37 at $H_{\rm LO}$ to 0.86 at $H_{\rm c2}$ for $\mu = 5$ in Fig. 4(b) and from 0.6 to 0.9 for $\mu = 2$ in Fig. 4(f).

C. Entropy

The H dependence of entropy $S_{\rm s}(T)/S_{\rm n}(T_{\rm c})$ is presented in Figs. 4(c) and 4(g) for $\mu = 5$ and $\mu = 2$, respectively. These behaviors show similar H dependence as in $\chi_{\rm spin}$ in Figs. 4(b) and 4(f). The entropy also shows a rapid increase in the LO state at $H_{\rm LO} < H < H_{\rm c2}$, and a small jump to the normal-state value 0.1 at $H_{\rm c2}$. In the LO state, $S_{\rm s}(T)/S_{\rm n}(T_{\rm c})$ changes from 0.035 to 0.084 for $\mu = 5$ in Fig. 4(c), and from 0.065 to 0.092 for $\mu = 2$ in Fig. 4(g). Quantitatively, $S_{\rm s}(T)/S_{\rm n}(T_{\rm c})$ is smaller by a factor of about 0.1 ($= T/T_{\rm c}$). Compared with $\chi_{\rm spin}$, $S_{\rm s}$ shows a small enhancement near $H_{\rm LO}$ in the Abrikosov state as seen in the insets.

D. Zero-energy DOS

Figures 4(d) and 4(h) show the H dependence of the zero-energy DOS $N(E = 0)$, which also shows similar

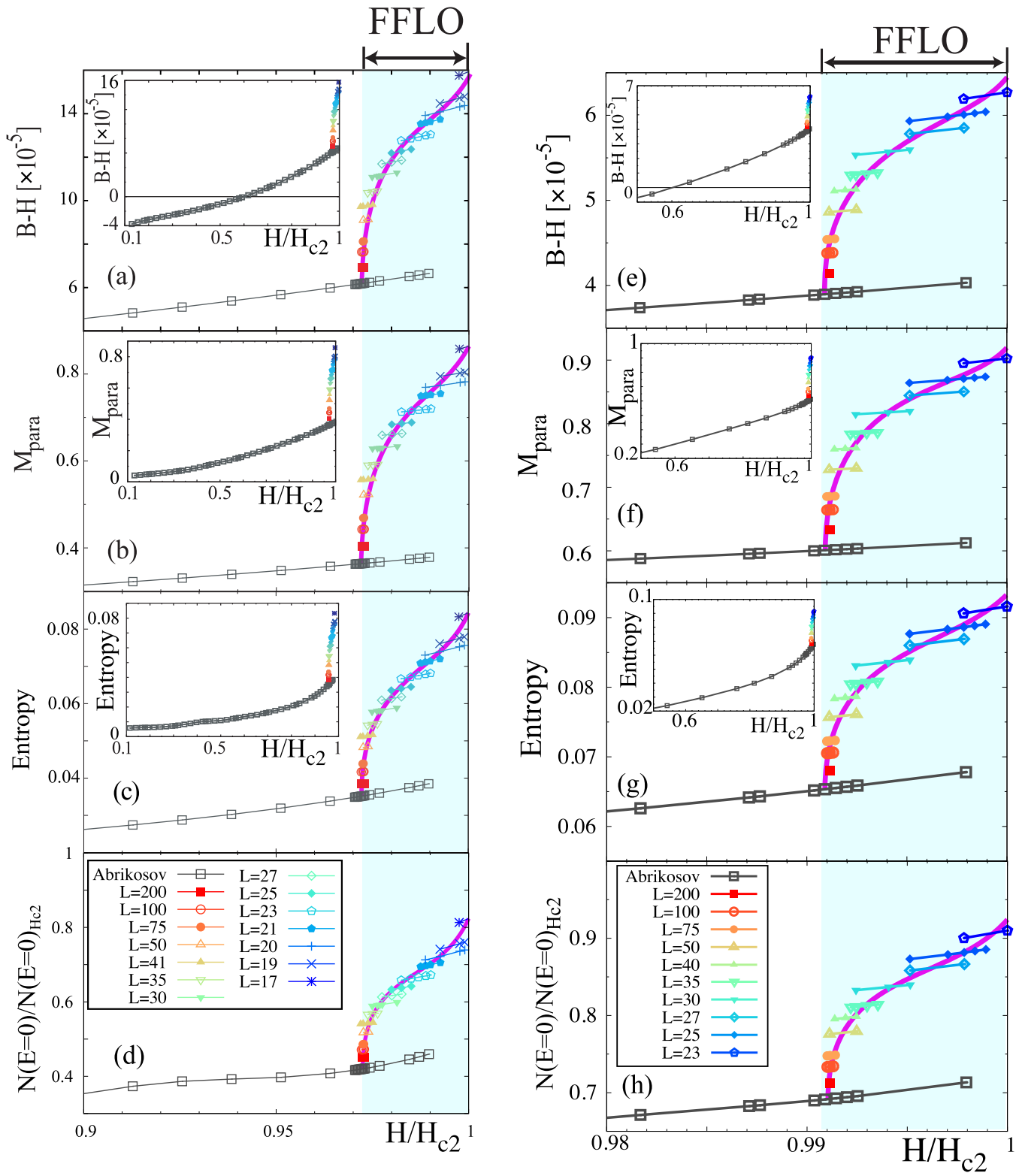

FIG. 4. (a) and (e) Magnetic field H dependence of magnetization $M = B - H$, (b) and (f) paramagnetic susceptibility $\chi_{\rm spin} = M_{\rm para}/M_0$, (c) and (g) entropy $S_{\rm s}(T)/S_{\rm n}(T_{\rm c})$, and (d) and (h) zero-energy DOS $\gamma = N(E=0)/N_0$. The left panels (a)–(d) are for $\mu = 5$, and right panels (e)–(h) for $\mu = 2$. $T = 0.1T_{\rm c}$. Insets in the upper three panels show the overall features in a wide range of H from low fields. Data points are plotted for L near the free energy minimum, with color presented in the lowest panels. Continuous curves are drawn as a guide for the eyes.

behavior to that of $\chi_{\rm spin}$ and $S_{\rm s}$ in the above panels in Fig. 4. The thermodynamic quantity also strongly increases with almost diverging slopes at $H_{\rm LO}$. In the LO state, $N(E=0)/N_0$ changes from 0.42 to 0.82 for $\mu=5$ in Fig. 4(d), and from 0.69 to 0.91 for $\mu=2$ in Fig. 4(h). The specific heat C is obtained by the derivative of $S_{\rm s}(T)$ as

$$C = T\frac{\partial S_{\rm s}}{\partial T}. \tag{9}$$

We note here that in the low-temperature limit C is evaluated as

$$\left(\frac{C}{T}\right)_{T\to 0} = \left(\frac{\partial S_{\rm s}}{\partial T}\right)_{T\to 0} = \frac{S_{\rm s}(T)-S_{\rm s}(0)}{T-0} = \frac{S_{\rm s}(T)}{T}, \tag{10}$$

that is, the Sommerfeld coefficient $\gamma(H)=C/T$ is directly related to the entropy,

$$\gamma(H) = \frac{S_{\rm s}(H)}{T} \tag{11}$$

at the low T limit. We roughly confirm this relation from the numerical results of $S_{\rm s}(H)$ and $\gamma(H)$ at $T=0.1T_{\rm c}$ in Fig. 4. The small deviations between them come from the effects of finite T. We also approximately confirm the relation $\chi_{\rm spin}(H)\sim\gamma(H)$ in Fig. 4. This relation is confirmed also in the LO state in addition to the Abrikosov state, which was proved for the latter state in previous studies [40,48,49]. Although the calculation of $\chi_{\rm spin}(H)$ is performed by Matsubara frequency ω_n, in the formulation of real energy E, $\chi_{\rm spin}(H)$ comes from the average of the DOS in the energy range $|E|<\mu H$ at low T. Thus, we have the relation $\chi_{\rm spin}(H)=\gamma(H)$ in the limit of weak Pauli paramagnetic effect, $\mu\to 0$, and low T. When μ is large, the deviation may appear between $\chi_{\rm spin}(H)$ and $\gamma(H)$.

As is seen above, we confirmed that thermodynamic quantities of magnetization, paramagnetic susceptibility, entropy, and low-temperature specific heat exhibit basically similar behaviors as a function of H. Namely, as H increases, the almost linear and monotonic increase suddenly shows a sharp rise at $H=H_{\rm LO}$ exhibiting a kink feature, but the thermodynamic quantities are continuous. Thus it is of second-order transition. This feature nicely corresponds to that in the analytic solutions [10,46], where at the tricritical Lifshitz point L diverges from the above.

Although it is difficult to check whether it is a second- or first-order transition, it is believed to be second order, judging from the analytic solutions [10,46]. However, it often happens that the actual experiments show the first-order transition because of other degrees of freedom such as phonons or lattice deformation involved. As for the phase transition at $H_{\rm c2}$, the rise terminates at $H=H_{\rm c2}$ abruptly via first-order-like jump.

Comparing the two cases for $\mu=5$ (left column) and $\mu=2$ (right column) in Fig. 4, it is seen that the former has a wider LO region than the latter. Otherwise, the two cases are quite similar, meaning that the qualitative features of the LO phase are independent of the μ parameter and thus universal. As μ decreases, the LO phase fades out from the H-T plane. Note that the critical μ is known to be $\mu_{\rm cr}=0.5$. Those thermodynamic quantities are expected to be measured by a variety of experiments, such as the specific heat at low T directly probes $N(0)$ and entropy. The paramagnetic moment is measured directly by a magnetization experiment, which was conducted in $CeCoIn_5$, giving similar overall characteristics [52] shown in Figs. 4(a) and 4(e) or by a SANS experiment through diffraction of the spatial variation of magnetization profile [53].

VI. FLL FORM FACTORS

A. Period $L(H)$ in the LO state

We first show the field evolution of the period L or the wave number $q=2\pi/L$ of the LO state before discussing the FLL form factors. As shown in Fig. 5(a) for $\mu=5$ and Fig. 5(e) for $\mu=2$, the wave number q of the stable LO state continuously varies with H. Starting with $q=0$ at $H=H_{\rm LO}$ where the LO period is infinity, q rises sharply whose tangent is almost diverging. Thus L becomes finite quickly. The antiphase solitonic wave form changes into a sinusoidal one upon increasing H [see also Fig. 3(a)]. This behavior is similar to that seen in the exact solution (see Fig. 9 in Ref. [10]), implying that the LO physics along the parallel direction exemplified here is common and universal, which was also pointed out in Ref. [15]. Comparing with the two cases $\mu=5$ in Fig. 5(a) and $\mu=2$ in Fig. 5(e) the $q(H)$ variation is somewhat rounded in $\mu=2$.

B. Fundamental form factor F_{100}

The FLL form factor is an important quantity that can be directly measured by SANS experiment. The form factors F_{hkl} with h, k, and l being integers are Fourier components of internal field $\mathbf{B}(\mathbf{r})$ in our calculation [17]. The fundamental Bragg spots F_{100} for the vortex lattice is shown in Fig. 5(b) for $\mu=5$ and Fig. 5(f) for $\mu=2$ as a function of H. The intensity $|F_{100}|^2$ increases in the Abrikosov state as seen from the insets in Figs. 5(b) and 5(f). This is because $M_{\rm para}(\mathbf{r})$ accumulates at the vortex core to increase $B(\mathbf{r})$ locally. This feature is already shown theoretically [40] and observed in various paramagnetically enhanced superconductors, such as in $TmNi_2B_2C$ [53] and $CeCoIn_5$ [24]. While the increase of $|F_{100}|^2$ as a function of H is greater for $\mu=5$ of the strong Pauli paramagnetic effect case, for the intermediate case $\mu=2$, $|F_{100}|^2$ shows a decrease at higher fields after the increase at lower fields.

As shown in the main panels of Figs. 5(b) and 5(f), the intensity of $|F_{100}|^2$ suddenly decreases upon entering the LO phase and keeps dropping quickly, almost exponentially. (Notice the $T=50$ mK data in Fig. 1 of Ref. [25].) This is because $B_z(\mathbf{r})$ is not enhanced at the vortex core on the LO nodal plane as seen from Fig. 2(c). This contribution decreases $|F_{100}|^2$, which is the average along the z axis. Comparing with the two cases $\mu=5$ in Fig. 5(b) and $\mu=2$ in Fig. 5(f), the $|F_{100}|^2$ variation in the LO state is somewhat rounded in $\mu=2$, similarly to the $q(H)$ behavior in Figs. 5(a) and 5(e). This indicates that the decrease of $|F_{100}|^2$ in the LO state is related to $q(H)=2\pi/L$, i.e., the volume weight of the LO nodal sheet in the superconductor. The other Bragg spots F_{hk0} (h, k integers) are associated with the vortex lattice, which characterize the detailed magnetic field distribution in the mixed state of a superconductor.

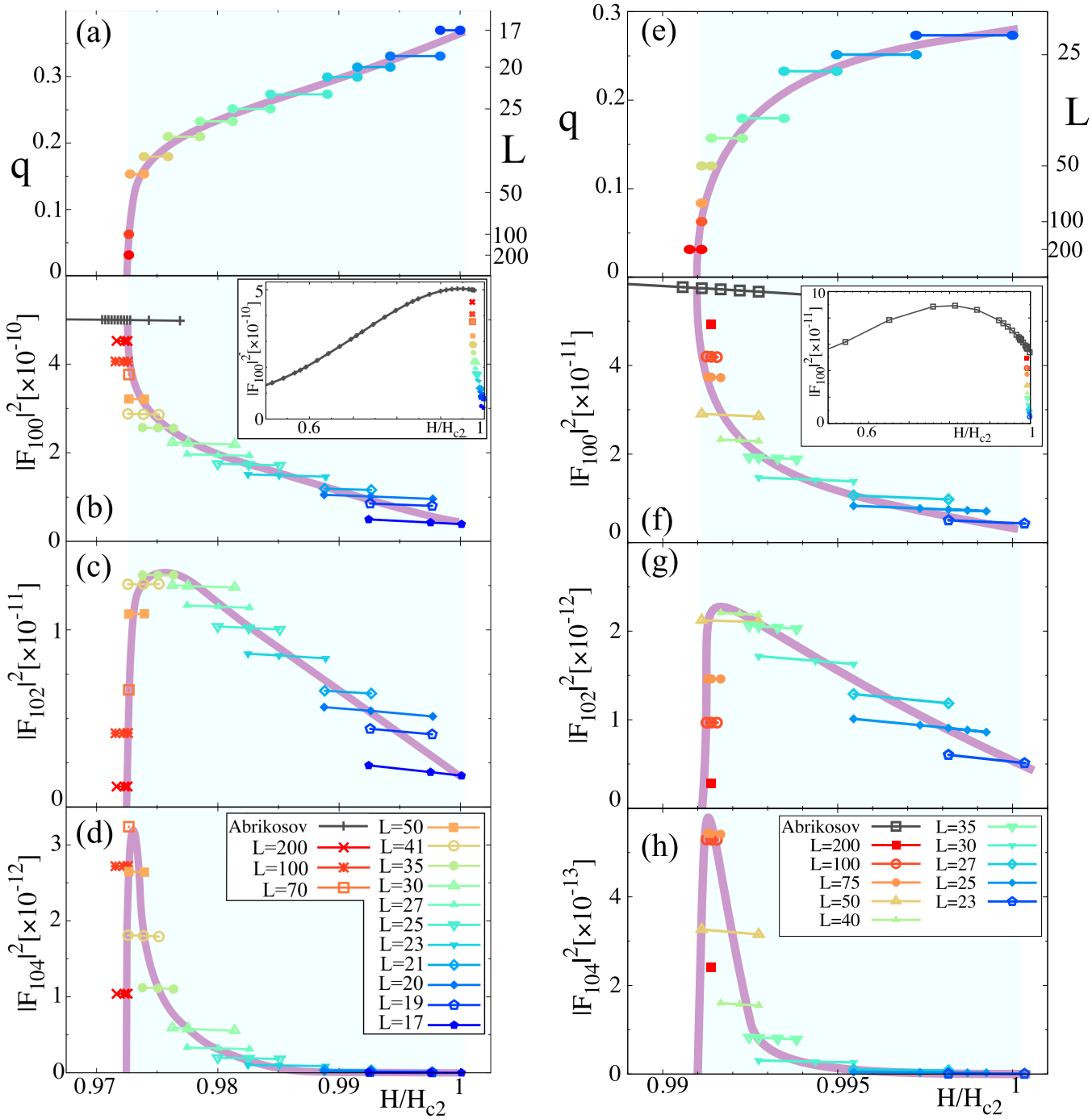

FIG. 5. Field evolutions of various quantities at $T/T_c = 0.1$ for $\mu = 5$ (left column) and $\mu = 2$ (right column). (a) and (e) LO wave number $q = 2\pi/L$. (b) and (f) Form factor $|F_{100}|^2$. Inset shows the overall variation. (c) and (g) Form factor $|F_{102}|^2$. (d) and (h) Form factor $|F_{104}|^2$. Data points are plotted for L near the free energy minimum, with color presented in the lowest panels. Continuous curves are drawn as a guide for the eyes.

C. Form factors F_{102} and F_{104} associated with LO state

The observation of extra spots F_{10n} ($n = 2, 4, \ldots$) is crucial to prove the existence of the LO phase. In Figs. 5(c) and 5(g) we show $|F_{102}|^2$, which is the superspot associated with the LO modulation along the field direction. $|F_{102}|^2$ rises sharply at $H = H_{LO}$. After taking a maximum in the middle of the LO phase, it slowly decreases toward H_{c2}. Note that $|F_{102}|^2$ behaves similarly for both $\mu = 5$ and $\mu = 2$ cases. Thus the results may not be sensitive to the μ value and generic. The best chance to observe the $|F_{102}|^2$ superspot is in the middle field region inside the LO phase. The relative intensity $|F_{102}|^2/|F_{100}|^2 = 1/10$–$1/20$ in both $\mu = 5$ and $\mu = 2$. It is possible to detect the F_{102} spot because $|F_{100}|^2$ is enhanced by the Pauli paramagnetic effect even near H_{c2}.

The higher-order spot $|F_{104}|^2$ is also shown in Figs. 5(d) and 5(h). It takes a maximum just near H_{LO}. Since the

magnitude of $|F_{104}|^2$ is further reduced compared with $|F_{102}|^2$ and is one order of magnitude smaller than $|F_{102}|^2$, it might be difficult to detect $|F_{104}|^2$. The μ parameter dependence of those form factors is qualitatively the same, only differing quantitatively.

From Figs. 5(c) and 5(d) for $\mu = 5$, with increasing H from $H_{\rm LO}$, the ratio $|F_{102}/F_{104}|^2$ is evaluated as $1.3 \times 10^{-12}/1.0 \times 10^{-12} = 1.3$ for $L = 200$, $6.8 \times 10^{-12}/3.2 \times 10^{-12} = 2.1$ for $L = 70$, and $1.3 \times 10^{-11}/1.1 \times 10^{-12} = 12$ for $L = 35$. From Figs. 5(g) and 5(h) for $\mu = 2$, the ratio $|F_{102}/F_{104}|^2$ is $2.8 \times 10^{-13}/2.4 \times 10^{-13} = 1.2$ for $L = 200$, $1.5 \times 10^{-12}/5.4 \times 10^{-13} = 2.8$ for $L = 75$, and $2.2 \times 10^{-12}/1.6 \times 10^{-13} = 14$ for $L = 40$. For both $\mu = 5$ and $\mu = 2$, the ratio $|F_{102}/F_{104}|^2$ rapidly increases from 1 at $H > H_{\rm LO}$. At higher H, as F_{104} becomes negligible, B_z distribution becomes a sinusoidal wave of F_{102} along the z direction.

VII. NMR SPECTRUM

In this section we examine the NMR spectrum which is also crucial to identify the LO state. Choosing probed nuclei that have different hyperfine coupling constants, we can measure the field distributions inside a superconductor [17]. When the hyperfine coupling is strong enough, the paramagnetic distribution $M_{\rm para}(\mathbf{r})$ is probed by NMR experiment. In the weak hyperfine coupling case the magnetic induction $B(\mathbf{r})$ in the whole system is detected by NMR. In the mixed state of ordinary superconductors it yields the so-called Redfield pattern. Here we analyze the field evolution of the NMR spectra for both strong and weak hyperfine coupling cases. For the former we evaluate the distribution $P(M)$ by using the stable LO state determined at each field. And for the latter the distribution $P(B)$ is calculated.

A. Paramagnetic distribution spectrum $P(M)$

We start with the strong hyperfine coupling constant case, which effectively probes the paramagnetic distribution $M_{\rm para}(\mathbf{r})$ in the system. The distribution $P(M)$ is given by

$$P(M) = \left\langle \delta\left(M - M_{\rm para}(\mathbf{r})\right)\right\rangle_{\mathbf{r}}, \tag{12}$$

i.e., the volume counting for each M. Figure 6(a) shows the spectral evolutions of the distribution $P(M)$.

Since in the Abrikosov state the paramagnetic moment is confined exclusively at the vortex cores, the single peak appears at the saddle point (S) position in the NMR spectrum. In the LO phase, $M_{\rm para}(\mathbf{r})$, which comes from excess electrons at the nodal sheets, accumulates near the normal state (N) position $M/M_0 = 1$. The peak near the N position becomes dominant toward H_{c2}, because the increasing excess unpaired quasiparticles appear at the LO nodal sheets as described above. It is noticed that just near $H = H_{\rm LO}$ two peaks with nearly equal height appear in the NMR spectrum in $P(M)$, and the noticeable spectral weight is seen at the higher $M_{\rm para}$ region. In addition to those characteristics, the spectral weight extends to higher values beyond M_0 near N positions. This comes from the increase of the domain wall contributions in the LO state as discussed below. Those features are important to characterize the spectra near the N position in the LO state as will be seen shortly in the last section.

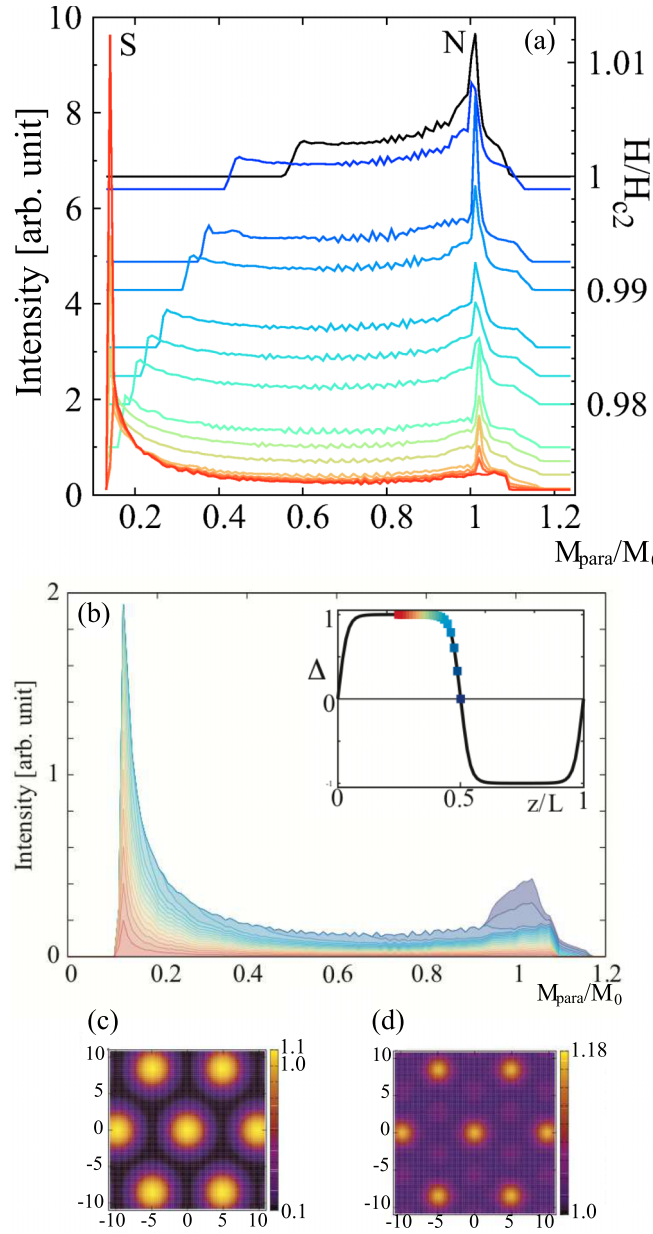

FIG. 6. NMR spectra $P(M)$ in the LO state. (a) Applied field H evolution of internal field distribution $P(M)$. $\mu = 5$ and $T/T_c = 0.1$. Horizontal baselines for each spectrum are shifted by H/H_{c2}, which is indicated on the right axis. (b) The z resolved the paramagnetic moment $M_{\rm para}$ distribution $P(M)$. Inset shows the order parameter profile as a function of z where color codes correspond to those in the main figure. (c) and (d) Density plots of paramagnetic moment $M_{\rm para}$ at the antinodal plane $z = 0.25L$ and at the nodal plane $z = 0.5L$, respectively. $T/T_c = 0.1$, $L = 75$, $H = 0.973H_{c2}$, and $\mu = 5$ for (b), (c), and (d).

The appearance of the double peaks at the S and near the N positions gives unambiguous evidence of the LO state. It may be possible to extract the wavelength L in the LO state by carefully examining the spectral evolution data because the spectral weights at S and N evolve continuously and gradually. In order to understand the physical meanings of those spectra $P(M)$ in Fig. 6(a) more deeply, we examine

the z-resolved $P(M)$ shown in Fig. 6(b). There the bulk superconducting contribution at the S point comes exclusively from the maximum position near $z = 0.25L$ of the order parameter amplitude. The normal contribution near the N point arises from the nodal plane at the middle $z = 0.5L$. The spectral distribution continuously evolves, depending on the order parameter spatial variation. The prominent double horn structure is a hallmark of the LO state and the spectral weights at the S and N points change, reflecting the field evolution of the LO state. Thus we can extract the information on the detailed LO spatial structure by carefully measuring the NMR spectrum.

As shown in Figs. 6(c) and 6(d) the cross-sectional views of the M profile at the antinodal plane and nodal plane, respectively, are displayed. Comparing those two cross-sectional views, it is seen that the vortex core contrast relative to the background is far clearer at the antinodal plane than that at the nodal plane. This is because the latter contrast is blurred by normal quasiparticles accumulated at the nodal plane. Note that the color range is $1.0 < M/M_0 < 1.18$ in Fig. 6(d), while $0.1 < M/M_0 < 1.1$ in Fig. 6(c). We point out here that according to the recent scanning tunneling microscopy (STM) measurement [54] on FeSe, which is a candidate material for the LO, under the perpendicular field to the surface the vortex images become suddenly invisible and bluer when entering the possible LO phase. This phenomenon can be understood in the following: At the surface where STM probes the electronic structure the nodal sheets are likely pinned there because of energetic consideration, thus as shown in Figs. 6(b) and 6(c) the contrast at the nodal sheet is by far lower than that at the antinodal plane. Since the paramagnetic moment is proportional to the DOS $N(E = 0)$, we anticipate that the same is happening for STM zero-bias images.

B. Magnetic induction distribution spectrum $P(B)$

Next we study the weak hyperfine coupling constant case, which probes effectively the magnetic induction distribution $P(B)$ in the whole system. The distribution $P(B)$ is given by

$$P(B) = \langle \delta(B - B(\mathbf{r})) \rangle_{\mathbf{r}}. \tag{13}$$

It is also important to observe the characteristic change of $P(B)$ as shown in Fig. 7(a). Note that $P(B)$ is probed, for example, at In(1) in $CeCoIn_5$ [20]. The double peak structure can be seen from Fig. 7(a) in the LO phase at $H > H_{LO}$, where the N peak appears near $B \sim H$ in the spectrum. Viewing the whole spectral shape in Fig. 7(a), the N position is situated near the S position in $P(B)$, compared with $P(M)$ in Fig. 6(a). In the lower field of the Abrikosov state, the usual Redfield pattern is reproduced as seen from Fig. 7(a). Thus the double peak structure at the N and S positions in $P(B)$ is a hallmark of the LO state. As H increases the relative spectral weight changes and eventually the spectral weight at N dominates the whole spectrum toward H_{c2}, which is shown in Fig. 7(a). Those eminent features of the NMR spectra in $P(B)$ can be useful and indispensable spectroscopic methods for identifying the LO state. Furthermore, it may be possible to extract the details of the LO state, such as the LO periodicity, by carefully examining those spectra.

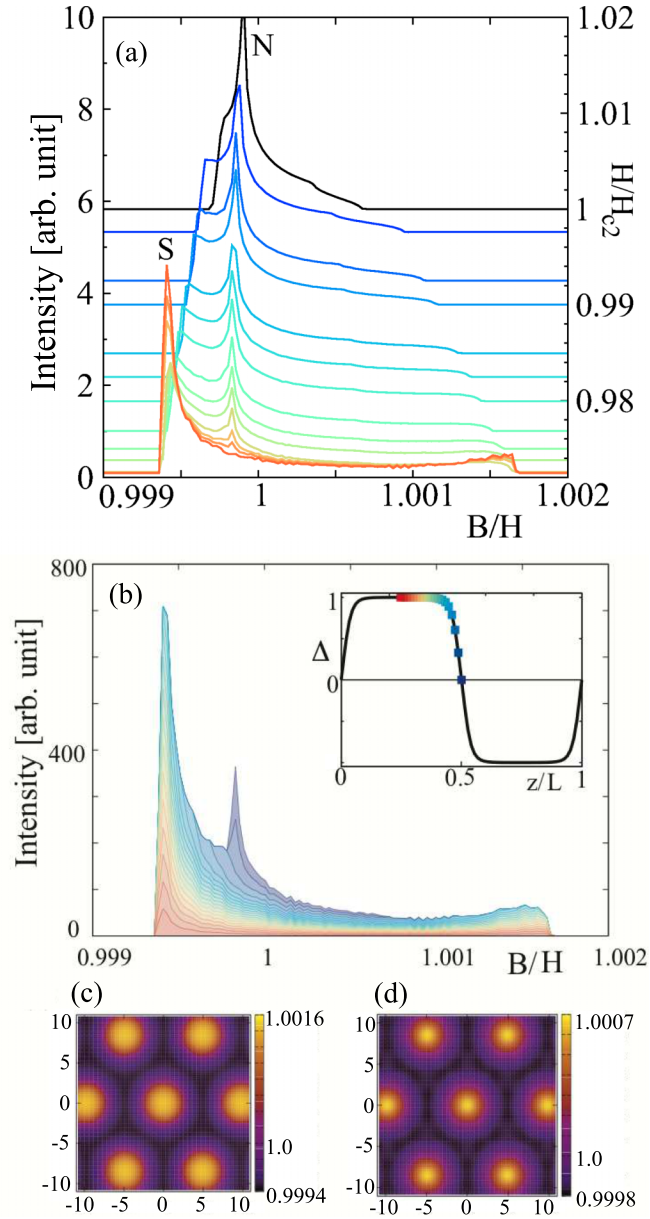

FIG. 7. NMR spectra $P(B)$ in the LO state. (a) Applied field H evolution of internal field distribution $P(B)$. $\mu = 5$ and $T/T_c = 0.1$. Horizontal baselines for each spectrum are shifted by H/H_{c2}, which is indicated on the right axis. (b) The z-resolved internal field B distribution $P(B)$. Inset shows the order parameter profile as a function of z where color codes correspond to those in the main figure. (c) and (d) Density plots of internal field B at the antinodal plane $z = 0.25L$ and at the nodal plane $z = 0.5L$, respectively. $T/T_c = 0.1$, $L = 75$, $H = 0.973H_{c2}$, and $\mu = 5$ for (b), (c), and (d).

As shown in Fig. 7(b) the double peak structure is analyzed by decomposing the spectral weight into the z-resolved $P(B)$. The peak of the S position comes from the contributions of the antinodal parts around $z/L = 0.25$, while that of the N position comes from the LO nodal sheet at $z/L = 0.5$ as seen in the inset of Fig. 7(b).

The cross-sectional views at the antinodal and nodal positions are displayed in Figs. 7(c) and 7(d), respectively. It is seen by comparing the scales that the contrast of the spectral

weight at the antinodal plane in Fig. 7(c) is far more visible than at the nodal plane in Fig. 7(d). This is the same as in the $P(M)$ case mentioned above.

VIII. DISCUSSIONS

Having calculated various physical properties of the stable LO states in detail, we now examine the possible experiments to identify the LO phase in several candidate materials, $SrRuO_4$, $CeCoIn_5$, $CeCu_2Si_2$, and the organic superconductors $(BEDT\text{-}TTF)_2X$ in light of the present theory.

A. Sr_2RuO_4

Sr_2RuO_4 was a prime candidate of the chiral p-wave superconductor. Much attention was focused on this symmetry. However, recent trends include the following: (1) first-order transition at $H_{c2}^{ab} \parallel ab$ found by the magnetocaloric effect [55], specific heat [56], and magnetization experiments [32]; (2) the intrinsic anisotropy 60 observed by SANS [57,58] as a vortex lattice deformation indicates that H_{c2} anisotropy $H_{c2}^{ab}/H_{c2}^{c} = 20$ is a suppressed value by the Pauli paramagnetic effect; (3) the absence of the split transition under uniaxial stresses [59], expected for chiral p-wave pairing belonging to a two-dimensional irreducible representation; and finally (4) the renewed Knight shift experiment [33] detects a decrease of the spin susceptibility below T_c for $H \parallel ab$. This demonstrates that the original results [60,61], which were one of the most important pieces of "evidence" for the spin-triplet pairing scenario, are in error due to heating effects by NMR pulses. This result is confirmed by the original researcher [62]. All recent results unambiguously point to the spin-singlet pairing under the strong Pauli effects. Therefore, it is quite reasonable to expect the LO state to realize in this "superclean" material. Moreover, its quasi-two-dimensional electronic structure is also favorable for it. Here we examine its possibility in light of the present calculations.

(a) According to the specific heat experiment data [63,64], $\gamma(H)$ at lower T exhibits an anomaly just before the first-order jump at $H_{c2}^{ab} = 1.5\,\mathrm{T}$ where almost linear and monotonous $\gamma(H)$ in H deviates upwardly around $H = 1.2\,\mathrm{T}$ at $T = 0.13\,\mathrm{K}$ [64]. This behavior is similar to Figs. 4(d) and 4(h). Thus we can identify $H_{\mathrm{LO}} \sim 1.2\,\mathrm{T}$ at that T.

(b) The ultrahigh resolution magnetostriction experiment [65] is performed and detects two successive anomalies as a function of H at low T, corresponding to H_{LO} and H_{c2}. The two first-order lines H_{LO} and H_{c2} merge at $H_{\mathrm{Lifshitz}} = 1.2\,\mathrm{T}$ and $T_{\mathrm{Lifshitz}} = 0.8\,\mathrm{K}$, which should be the tricritical Lifshitz point. Thus the constructed phase diagram is consistent with our Figs. 1(b) and 1(d) qualitatively. Note that the angle-resolved specific heat measurement [66] also detects the anomalous oscillation sign change at higher H regions, signaling the LO phase.

(c) One of the most direct visualizations of the LO state is to use STM measurement under parallel fields. As shown in Fig. 2 (also see Fig. 6 in Ref. [17]), the nodal plane can be imaged as a distinctive stripe structure near the zero-bias energy region in STM-STS (scanning tunneling spectroscopy) experiments. This stripe image is best observed under an applied field parallel to the surface of the ab plane where the vortices lie near the surface. The estimated stripe distance varies, depending on the field strength as seen from Figs. 1(a) and 1(c), typically $L = 20\xi \sim 200\,\mathrm{nm}$ with $\xi \sim 10\,\mathrm{nm}$. Since in this STM parallel configuration the vortex lattices are successfully imaged before in $2H$-$NbSe_2$ [67–69], this can be a feasible experiment on Sr_2RuO_4 in which STM experiment is done [70].

(d) According to the recent ^{17}O-NMR experiment [71], the NMR spectrum is split at around $H = 1.35\,\mathrm{T}$ and $T = 0.07\,\mathrm{K}$ for the in-plane field. This double horn spectrum is akin to our result shown in Fig. 6. The corresponding H-T region also coincides roughly with the LO phase diagram given by Kittaka *et al.* [63].

(e) The $\mathbf{q}$-vector direction of the LO state is anticipated in Sr_2RuO_4 as follows: There are three bands α, β, and γ. The first two have squared cross-sectional shapes in the ab plane, while the γ Fermi surface is somewhat rounded. The best nesting for the LO phase is that the $\mathbf{q}$ vector points to the (110) direction rather than (100) because the (110) direction nests two sides of the squared Fermi surface simultaneously and is more advantageous than (100). This can be confirmed by calculating the superconducting susceptibility based on a first-principles band calculation [72]. Since the $\mathbf{q}$ vector is fixed to either (110) or $(1\bar{1}0)$ under the in-plane H, it happens that when rotating H in the ab plane a switching phenomenon from (110) or $(1\bar{1}0)$ may be observed, similar to that observed in $CeCoIn_5$ [73,74].

(f) The SANS experiments on Sr_2RuO_4 done so far [57,58] only probe the transverse component relative to the field direction nearly applied to the ab plane. The Pauli paramagnetic effect manifests itself in the longitudinal component which is discussed above. Thus the existing data do not provide us the information on the LO state. In principle, it is possible to perform the SANS experiment to see the longitudinal component. At present the low neutron flux intensity and/or the uniformity of the applied magnetic field [75] prevent us from observing it.

B. $CeCoIn_5$

The heavy-fermion superconductor $CeCoIn_5$ is one of the prime candidates for realizing the LO state. Many experimental and theoretical works have been already devoted to studying it in this respect and accumulated several important clues for the LO state. Here in the light of the present theory, we examine its possibility and propose further experimental and theoretical verifications toward this end.

$CeCoIn_5$ is known for a superconductor with strong Pauli paramagnetic effect because of the strong H_{c2} suppression [76], the first-order transitions at H_{c2} both for $H \parallel ab$ and $H \parallel c$ observed by specific heat [21], and magnetization [52] measurements. This system is favorable for the LO state since the coherence length is short ($\xi^{ab} = 8.2\,\mathrm{nm}$ and $\xi^{c} = 3.5\,\mathrm{nm}$) due to heavy effective mass compared to the mean free path $l \sim 1000\,\mathrm{nm}$, thus it is a clean system, and the Maki parameter $\mu \sim 10$ is large enough. Thus it is legitimate to seek the LO state in this material. Since for $H \parallel ab$, the situation is complicated by the existence of the so-called Q phase [22,73], which is a mixture of the antiferromagnetism and LO state, we mainly focus on the simpler case of $H \parallel c$.

1. NMR

We first discuss the NMR experiments on $CeCoIn_5$ [19,20]. The observed double peak structure of In(2a) of the NMR spectra for $H \parallel c$ and for $H \parallel ab$ is remarkably similar to our Fig. 6(a) (see the spectral evolutions in Fig. 1 of Ref. [19] and Fig. 2 of Ref. [20]). The proposed phase diagram of the LO state for $H \parallel c$ is also similar to our Figs. 1(b) and 1(d) where $H_{\rm LO}/H_{c2} \sim 0.975$ for $\mu = 5$ compared with $H_{\rm LO}/H_{c2} = 4.7\,{\rm T}/4.95\,{\rm T} \sim 0.95$ at low temperatures for $H \parallel c$ [19]. As mentioned before the value of $H_{\rm LO}/H_{c2}$ depends on μ, but the topological shape of the LO phase diagram is hardly changed as compared with Fig. 1(b) for $\mu = 5$ and Fig. 1(d) for $\mu = 2$. In this connection, for $H \parallel ab$ the proposed phase diagram (see Fig. 3 of Ref. [20]) is quite modified because of the presence of the existing spin-density wave (SDW) whose origin is debated. Generally heavy-fermion superconductors have a tendency to SDW instability [77,78].

We also point out that the observed $M_{\rm para}(H)$ (see Fig. 4 of Ref. [20]), which shows a strong rise at the onset of the LO state, is again very similar to our results in Figs. 4(c) and 4(f). Therefore, judging from those features, the spectral shape and the field evolution of $M_{\rm para}(H)$, we conclude that in the high fields for $H \parallel c$ the genuine LO phase is realized in this system.

2. Entropy and specific heat

In order to confirm this identification, we consider other thermodynamic measurements. Tokiwa *et al.* [79] measured the specific heat and the magnetocaloric effect and found a kink in the entropy $dS(H)/dH$ at $H \sim 4.4\,{\rm T}$ of $T = 0.2$ K, which coincides with the expected LO phase diagram. However, the calculated $S(H)$ behaviors shown in Figs. 4(c) and 4(g) are not reproduced precisely. This origin is not known at this moment.

3. SANS

White *et al.* [25] performed the SANS experiment for $H \parallel c$ and studied the vortex lattice structure in this system. Apart from interesting vortex lattice symmetry changes as a function of H, they observe the fundamental form factor $F_{100}(H)$ (see Fig. 1 in Ref. [25]), which is favorably compared with the insets of Figs. 5(b) and 5(f). Namely, $F_{100}(H)$ gradually increases and suddenly drops just before H_{c2}, which should be contrasted with the ordinary type-II superconductors with the monotonous and exponential decrease of $F_{100}(H)$.

So far, the detailed SANS observation inside the LO phase is not done yet. There is no data for other form factors to be compared, in particular $F_{102}(H)$ of Figs. 5(c) and 5(g), which are a hallmark of the LO state. Here we point out the feasibility to observe $F_{102}(H)$ in this system. According to our calculations shown in Fig. 5, the anticipated intensity of $|F_{102}|^2$ is one or two orders of magnitude smaller than $|F_{100}|^2$. We emphasize that this intensity is already covered by the $|F_{100}|^2$ observation [25], meaning that $|F_{102}|^2$ can be detected by the present facility and is quite feasible. Thus we challenge SANS experimentalists to perform it in order to establish the LO state unambiguously.

4. STM

One of the most difficult tasks for STM experiment is to prepare a high-quality surface, which is not always possible, depending on materials. $CeCoIn_5$ is fortunate because the STM-STS measurements are already performed [80,81] and are guaranteed to prepare a good surface. Then we propose the same parallel field STM-STS measurement to observe the nodal stripe structure associated with the LO state discussed earlier. Since judging from the amplitude of the paramagnetic moment jump at H_{c2} the thermodynamic signature of the LO state in $CeCoIn_5$ is far clearer than that in Sr_2RuO_4, we understand that $CeCoIn_5$ is the best candidate for confirming the LO state by STM-STS too.

C. $CeCu_2Si_2$

Kitagawa *et al.* [27] have performed NMR measurements on $CeCu_2Si_2$ and found that $1/TT_1$ as a function of H enhances just near H_{c2}. Since $1/TT_1 \propto N(E=0)^2$, this behavior is similar to that of the LO phase shown in Figs. 4(d) and 4(h). This lets the authors claim the evidence for the LO state. It is true that this system is under strong Pauli paramagnetic effect because of the severe H_{c2} suppression observed. However, in view of high residual resistance at lower T, meaning that the mean free path is short and of multiband nature, the LO interpretation must be cautious. In fact, we argue [28] that the absence of the first-order transition at H_{c2} in this system can be understood in terms of the interplay of multibands, which otherwise hides the first-order transition expected for a single band. We also point out that the zero-energy DOS $N(E=0)$ can be enhanced more than the normal DOS at high H, which could explain the enhanced $1/TT_1$ phenomenon. Indeed this is observed in the specific heat experiment [82]. This is consistent with the STM observation [83] too. Thus we conclude that there is no evidence for the LO state in $CeCu_2Si_2$.

D. $(BEDT\text{-}TTF)_2X$

The organic superconductors $(BEDT\text{-}TTF)_2X$ [$X = Cu(NCS)_2$ [26,84–87] and $SF_5CH_2CF_2SO_3$ [88,89]] are ideal candidates for the LO state. The first-order phase transition at H_{c2} is observed by the specific heat [84] and magnetic torque [85] measurements in $X = Cu(NCS)_2$. Agosta *et al.* [87] measured the field-dependent specific heat and found a sharp increase of it similar to our Figs. 4(d) and 4(h) where at the onset field $H_{\rm LO}$, the phase transition is found to be of first order with hysteresis. This behavior is also backed up by a NMR experiment [26] where $1/TT_1$ as a function of H enhances just near H_{c2}. The phase diagram obtained [87] with the enhanced H_{c2} and wider LO region is somewhat different from those in Figs. 1(b) and 1(d). This difference may come from the different vortex nature in this organic superconductor. It is the Josephson-type vortex without a vortex core, and only the phase is winding around. Thus the orbital depairing effect is less severe here, stabilizing the LO at higher fields compared with our case. Since no one succeeded in microscopically describing the Josephson vortex nature, it is difficult to reproduce the LO phase diagram. The situation may be more akin to the cases without orbital

depairing. In fact, according to Machida and Nakanishi [10], the phase diagram with diverging H_{c2} is similar to that obtained experimentally [87], although the divergence itself is an artifact due to quasi-1D band modeling, but the tendency captures the essential point.

As for $X = SF_5CH_2CF_2SO_3$, the phase diagram is obtained [88], which is similar to our Figs. 1(b) and 1(d), but the LO region is much wider than ours. The estimated LO wavelength [89] normalized by the coherence length is 2.2–13.1, which is somewhat shorter than our estimate in Figs. 5(a) and 5(e).

IX. CONCLUSION

We quantitatively explore the field evolution of the LO states for the typical and canonical example of 3D Fermi sphere and *s*-wave pairing, by self-consistently solving the microscopic Eilenberger equation in the 3D space of the vortex lattice and the LO modulation along the field direction. Our calculation, which is reliable in the quantitative level, fully considers the Pauli paramagnetic and orbital depairing effects simultaneously. In order to facilitate the identification of the LO state by experiments, we estimate the H-T phase diagram, NMR spectrum, FLL form factors by SANS, and other thermodynamic quantities, such as paramagnetic moment, entropy, and zero-energy density of states as a function of the magnetic field in FFLO vortex states. We compare the two cases of strong and intermediate Pauli paramagnetic effect. We also discuss several candidate materials in the light of the present theory.

There are several issues that are not covered here: the effects of Fermi surface dimensionality; 3D versus 2D where magnetic field direction relative to the Fermi surface anisotropy becomes important [90], leading to a different phase diagram and different nature of the phase transitions. This remark is particularly true for Sr_2RuO_4, $CeCoIn_5$, and $(BEDT\text{-}TTF)_2Cu(NCS)_2$ as these materials are known to have quasi-2D Fermi surfaces. Here we confined ourselves to the LO state, but the FF state [47] is left untouched.

ACKNOWLEDGMENTS

We thank T. Sakakibara, S. Kittaka, Y. Shimizu, M. R. Eskildsen, N. Kikugawa, S. Yonezawa, K. Ishida, and S. Kitagawa for useful discussions on the experimental side, and N. Nakai, T. Mizushima, M. Takahashi, Y. Amano, and M. Ishihara for their collaborations at the earlier stage of this project. This work is supported by JSPS KAKENHI, Grant No. 17K05553 and partly performed at the Aspen Center for Physics, which is supported by National Science Foundation Grant No. PHY-1607611.

[1] P. Fulde and R. A. Ferrell, Phys. Rev. **135**, A550 (1964).
[2] A. I. Larkin and Y. N. Ovchinnikov, Zh. Eksp. Teor. Fiz. **47**, 1136 (1964) [Sov. Phys. JETP 20, 762 (1965)].
[3] See, for review, Y. Matsuda and H. Shimahara, J. Phys. Soc. Jpn. **76**, 051005 (2007).
[4] T. Mizushima, K. Machida, and M. Ichioka, Phys. Rev. Lett. **94**, 060404 (2005).
[5] K. Machida, T. Mizushima, and M. Ichioka, Phys. Rev. Lett. **97**, 120407 (2006).
[6] M. W. Zwierlein, A. Schirotzek, C. H. Schunck, and W. Ketterle, Science **311**, 492 (2006).
[7] M. W. Zwierlein, C. H. Schunck, A. Schirotzek, and W. Ketterle, Nature (London) **442**, 54 (2006).
[8] G. B. Partridge, W. Li, R. I. Kamar, Y. Liao, and R. G. Hulet, Science **311**, 503 (2006).
[9] S. Takada and T. Izuyama, Prog. Theor. Phys. **41**, 635 (1984).
[10] K. Machida and H. Nakanishi, Phys. Rev. B **30**, 122 (1984).
[11] S. Matsuo, H. Shimahara, and K. Nagai, J. Phys. Soc. Jpn. **64**, 371 (1995).
[12] H. Shimahara, J. Phys. Soc. Jpn. **67**, 736 (1998).
[13] A. B. Vorontsov, J. A. Sauls, and M. J. Graf, Phys. Rev. B **72**, 184501 (2005).
[14] L. W. Gruenberg and L. Gunther, Phys. Rev. Lett. **16**, 996 (1966).
[15] M. Tachiki, S. Takahashi, P. Gegenwart, M. Weiden, M. Long, C. Geibel, F. Steglich, M. Modler, C. Paulsen, and Y. Ōnuki, Z. Phys. B **100**, 369 (1997).
[16] R. Ikeda and H. Adachi, Phys. Rev. B **69**, 212506 (2004).
[17] M. Ichioka, H. Adachi, T. Mizushima, and K. Machida, Phys. Rev. B **76**, 014503 (2007).
[18] B.-L. Young, R. R. Urbano, N. J. Curro, J. D. Thompson, J. L. Sarrao, A. B. Vorontsov, and M. J. Graf, Phys. Rev. Lett. **98**, 036402 (2007).
[19] K. Kumagai, M. Saitoh, T. Oyaizu, Y. Furukawa, S. Takashima, M. Nohara, H. Takagi, and Y. Matsuda, Phys. Rev. Lett. **97**, 227002 (2006).
[20] K. Kumagai, H. Shishido, T. Shibauchi, and Y. Matsuda, Phys. Rev. Lett. **106**, 137004 (2011).
[21] A. Bianchi, R. Movshovich, C. Capan, P. G. Pagliuso, and J. L. Sarrao, Phys. Rev. Lett. **91**, 187004 (2003).
[22] M. Kenzelmann, Th. Strässle, C. Niedermayer, M. Sigrist, B. Padmanabhan, M. Zolliker, A. D. Bianchi, R. Movshovich, E. D. Bauer, J. L. Sarrao, and J. D. Thompson, Science **321**, 1652 (2010).
[23] M. Kenzelmann, S. Gerber, N. Egetenmeyer, J. L. Gavilano, Th. Strässle, A. D. Bianchi, E. Ressouche, R. Movshovich, E. D. Bauer, J. L. Sarrao, and J. D. Thompson, Phys. Rev. Lett. **104**, 127001 (2010).
[24] A. D. Bianchi, M. Kenzelmann, L. DeBeer-Schmitt, J. S. White, E. M. Forgan, J. Mesot, M. Zolliker, J. Kohlbrecher, R. Movshovich, E. D. Bauer, J. L. Sarrao, Z. Fisk, C. Petrović, and M. R. Eskildsen, Science **319**, 177 (2008).
[25] J. S. White, P. Das, M. R. Eskildsen, L. DeBeer-Schmitt, E. M. Forgan, A. D. Bianchi, M. Kenzelmann, M. Zolliker, S. Gerber, J. L. Gavilano, J. Mesot, R. Movshovich, E. D. Bauer, J. L. Sarrao, and C. Petrovic, New J. Phys. **12**, 023026 (2010).
[26] H. Mayaffre, S. Krämer, M. Horvatić, C. Berthier, K. Miyagawa, K. Kanoda, and V. F. Mitrović, Nat. Phys. **10**, 928 (2014).
[27] S. Kitagawa, G. Nakamine, K. Ishida, H. S. Jeevan, C. Geibel, and F. Steglich, Phys. Rev. Lett. **121**, 157004 (2018).

[28] Y. Tsutsumi, K. Machida, and M. Ichioka, Phys. Rev. B **92**, 020502(R) (2015).
[29] A. P. Mackenzie and Y. Maeno, Rev. Mod. Phys. **75**, 657 (2003).
[30] Y. Maeno, S. Kittaka, T. Nomura, S. Yonezawa, and K. Ishida, J. Phys. Soc. Jpn. **81**, 011009 (2012).
[31] K. Machida, K. Irie, K. Suzuki, H. Ikeda, and Y. Tsutsumi, Phys. Rev. B **99**, 064510 (2019).
[32] S. Kittaka, A. Kasahara, T. Sakakibara, D. Shibata, S. Yonezawa, Y. Maeno, K. Tenya, and K. Machida, Phys. Rev. B **90**, 220502 (R) (2014).
[33] A. Pustogow, Yongkang Luo, A. Chronister, Y.-S. Su, D. A. Sokolov, F. Jerzembeck, A. P. Mackenzie, C. W. Hicks, N. Kikugawa, S. Raghu, E. D. Bauer, and S. E. Brown, Nature (London) **574**, 72 (2019).
[34] G. Eilenberger, Z. Phys. **214**, 195 (1968).
[35] K. M. Suzuki, Y. Tsutsumi, N. Nakai, M. Ichioka, and K. Machida, J. Phys. Soc. Jpn. **80**, 113702 (2011).
[36] M. Ichioka, N. Hayashi, and K. Machida, Phys. Rev. B **55**, 6565 (1997).
[37] P. Miranović, N. Nakai, M. Ichioka, and K. Machida, Phys. Rev. B **68**, 052501 (2003).
[38] M. Ichioka, A. Hasegawa, and K. Machida, Phys. Rev. B **59**, 184 (1999).
[39] M. Ichioka, A. Hasegawa, and K. Machida, Phys. Rev. B **59**, 8902 (1999).
[40] M. Ichioka and K. Machida, Phys. Rev. B **76**, 064502 (2007).
[41] K. Watanabe, T. Kita, and M. Arai, Phys. Rev. B **71**, 144515 (2005).
[42] M. Hiragi, K. M. Suzuki, M. Ichioka, and K. Machida, J. Phys. Soc. Jpn. **79**, 094709 (2010).
[43] M. M. Doria, J. E. Gubernatis, and D. Rainer, Phys. Rev. B **41**, 6335 (1990).
[44] T. Mizushima, M. Takahashi, and K. Machida, J. Phys. Soc. Jpn. **83**, 023703 (2014).
[45] M. Takahashi, T. Mizushima, and K. Machida, Phys. Rev. B **89**, 064505 (2014).
[46] K. Machida and M. Fujita, Phys. Rev. B **30**, 5284 (1984).
[47] V. Zhuravlev and T. Maniv, Phys. Rev. B **80**, 174520 (2009).
[48] K. Machida and M. Ichioka, Phys. Rev. B **77**, 184515 (2008).
[49] Y. Amano, M. Ishihara, M. Ichioka, N. Nakai, and K. Machida, Phys. Rev. B **91**, 144513 (2015).
[50] Y. Amano, M. Ishihara, M. Ichioka, N. Nakai, and K. Machida, Phys. Rev. B **90**, 144514 (2014).
[51] N. Nakai and K. Machida, Phys. Rev. B **92**, 054505 (2015).
[52] T. Tayama, A. Harita, T. Sakakibara, Y. Haga, H. Shishido, R. Settai, and Y. Onuki, Phys. Rev. B **65**, 180504(R) (2002).
[53] L. DeBeer-Schmitt, M. R. Eskildsen, M. Ichioka, K. Machida, N. Jenkins, C. D. Dewhurst, A. B. Abrahamsen, S. L. Bud'ko, and P. C. Canfield, Phys. Rev. Lett. **99**, 167001 (2007).
[54] T. Hanaguri (private communication).
[55] S. Yonezawa, T. Kajikawa, and Y. Maeno, Phys. Rev. Lett. **110**, 077003 (2013).
[56] S. Yonezawa, T. Kajikawa, and Y. Maeno, J. Phys. Soc. Jpn. **83**, 083706 (2014).
[57] C. Rastovski, C. D. Dewhurst, W. J. Gannon, D. C. Peets, H. Takatsu, Y. Maeno, M. Ichioka, K. Machida, and M. R. Eskildsen, Phys. Rev. Lett. **111**, 087003 (2013).
[58] S. J. Kuhn, W. Morgenlander, E. R. Louden, C. Rastovski, W. J. Gannon, H. Takatsu, D. C. Peets, Y. Maeno, C. D. Dewhurst, J. Gavilano, and M. R. Eskildsen, Phys. Rev. B **96**, 174507 (2017).
[59] C. A. Watson, A. S. Gibbs, A. P. Mackenzie, C. W. Hicks, and K. A. Moler, Phys. Rev. B **98**, 094521 (2018).
[60] K. Ishida, H. Mukuda, Y. Kitaoka, K. Asayama, Z. Q. Mao, Y. Mori, and Y. Maeno, Nature (London) **396**, 658 (1998).
[61] K. Ishida, H. Mukuda, Y. Kitaoka, Z. Q. Mao, H. Fukazawa, and Y. Maeno, Phys. Rev. B **63**, 060507(R) (2001).
[62] K. Ishida, M. Manago, and Y. Maeno, J. Phys. Soc. Jpn. **89**, 034712 (2020).
[63] S. Kittaka (private communication).
[64] S. Yonezawa (private communication).
[65] S. Kittaka, T. Sakakibara, N. Kikugawa, T. Terashima, S. Uji, D. A. Sokolov, and K. Machida (unpublished).
[66] S. Kittaka, S. Nakamura, T. Sakakibara, N. Kikugawa, T. Terashima, S. Uji, D. A. Sokolov, A. P. Mackenzie, K. Irie, Y. Tsutsumi, K. Suzuki, and K. Machida, J. Phys. Soc. Jpn. **87**, 093703 (2018).
[67] H. F. Hess, C. A. Murray, and J. V. Waszczak, Phys. Rev. B **50**, 16528 (1994).
[68] J. A. Galvis, E. Herrera, C. Berthod, S. Vieira, I. Guillarmón, and H. Suderow, Commun. Phys. **1**, 30 (2018).
[69] I. Fridman, C. Kloc, C. Petovic, and J. Y. T. Wei, Appl. Phys. Lett. **99**, 192505 (2011).
[70] I. A. Firmo, S. Lederer, C. Lupien, A. P. Mackenzie, J. C. Davis, and S. A. Kivelson, Phys. Rev. B **88**, 134521 (2013).
[71] K. Ishida (private communication).
[72] K. Suzuki (private communication).
[73] S. Gerber, M. Bartkowiak, J. L. Gavilano, E. Ressouche, N. Egetenmeyer, C. Niedermayer, A. D. Bianchi, R. Movshovich, E. D. Bauer, J. D. Thompson, and M. Kenzelmann, Nat. Phys. **10**, 126 (2014).
[74] D. Y. Kim, Shi-Zeng Lin, F. Weickert, E. D. Bauer, F. Ronning, J. D. Thompson, and R. Movshovich, Phys. Rev. Lett. **118**, 197001 (2017).
[75] M. R. Eskildsen (private communication).
[76] S. Ikeda, H. Shishido, M. Nakamura, R. Settai, D. Aoki, Y. Haga, H. Harima, Y. Aoki, T. Namiki, H. Sato, and Y. Onuki, J. Phys. Soc. Jpn. **70**, 2248 (2001).
[77] K. Machida and M. Kato, Phys. Rev. Lett. **58**, 1986 (1987).
[78] K. M. Suzuki, M. Ichioka, and K. Machida, Phys. Rev. B **83**, 140503(R) (2011).
[79] Y. Tokiwa, E. D. Bauer, and P. Gegenwart, Phys. Rev. Lett. **109**, 116402 (2012).
[80] B. B. Zhou, S. Misra, E. H. da Silva Neto, P. Aynajian, R. E. Baubach, J. D. Thompson, E. D. Buer, and A. Yazdani, Nat. Phys. **9**, 474 (2013),
[81] A. Gyenis, B. E. Feldman, M. T. Randeria, G. A. Peterson, E. D. Bauer, P. Aynajian, and A. Yazdani, Nat. Commun. **9**, 549 (2018).
[82] S. Kittaka, Y. Aoki, Y. Shimura, T. Sakakibara, S. Seiro, C. Geibel, F. Steglich, H. Ikeda, and K. Machida, Phys. Rev. Lett. **112**, 067002 (2014).
[83] M. Enayat, Z. Sun, A. Maldonado, H. Suderow, S. Seiro, C. Geibel, S. Wirth, F. Steglich, and P. Wahl, Phys. Rev. B **93**, 045123 (2016).
[84] R. Lortz, Y. Wang, A. Demuer, P. H. M. Böttger, B. Bergk, G. Zwicknagl, Y. Nakazawa, and J. Wosnitza, Phys. Rev. Lett. **99**, 187002 (2007).
[85] B. Bergk, A. Demuer, I. Sheikin, Y. Wang, J. Wosnitza, Y. Nakazawa, and R. Lortz, Phys. Rev. B **83**, 064506 (2011).

[86] J. A. Wright, E. Green, P. Kuhns, A. Reyes, J. Brooks, J. Schlueter, R. Kato, H. Yamamoto, M. Kobayashi, and S. E. Brown, Phys. Rev. Lett. **107**, 087002 (2011).

[87] C. C. Agosta, N. A. Fortune, S. T. Hannahs, S. Gu, L. Liang, J.-H. Park, and J. A. Schleuter, Phys. Rev. Lett. **118**, 267001 (2017).

[88] S. Sugiura, T. Isono, T. Terashima, S. Yasuzuka, J. A. Schlueter, and S. Uji, npj Quantum Mater. **4**, 7 (2019).

[89] S. Sugiura, T. Terashima, S. Uji, S. Yasuzuka, and J. A. Schlueter, Phys. Rev. B **100**, 014515 (2019).

[90] K. W. Song and A. E. Koshelev, Phys. Rev. X **9**, 021025 (2019).